Development of pore water pressure during freeze-thaw cycles in weather conditions

Fukui, Kazuma

Iba, Chiemi

Development of pore water pressure during freeze-thaw cycles in weather conditions

Kazuma Fukui[a,] ***and Chiemi Iba**[b]

[a]Kobe University, Graduate School of Engineering, 1-1, Rokkodai-cho, Nada-ku, Kobe, 657-8501, Japan

[b]Kyoto University, Graduate School of Engineering, Kyotodaigaku-katsura, Nishikyo-ku, Kyoto, 615-8540, Japan

Abstract. To assess the risk of frost damage to building materials, the mechanisms of pressure development in a material due to freezing under weather conditions should be adequately understood. In this study, we have demonstrated the evolution of pore water pressure in a brick wall during cyclic freezing and thawing caused by changes in air temperature and solar radiation. We developed a coupled hygrothermal and mechanical model of brick walls based on the theory of poromechanics. The calculation results showed that the water pressure in a south facing wall increases significantly during the night in a cold region. For a south facing wall, the surface thaws during the day due to solar radiation and freezes again at night, while the interior remains frozen throughout the day. We conclude that such incomplete freeze-thaw cycles in the weather conditions are much more damaging to building materials than a monotonous repetition of complete freezing and thawing.

Keywords: Frost damage, masonry, numerical simulation, weather condition, solar radiation, poromechanics

1. Introduction

Assessing the risk of deterioration of buildings and structures is of great importance in achieving sustainable development. Frost action is one of the main causes of such deterioration, and considerable efforts have been made to assess the risks of frost damage associated with weather conditions. Such

*Corresponding author: fukui@peridot.kobe-u.ac.jp

studies have been conducted mainly using various indexes reflecting environmental conditions, such as the number of freeze-thaw cycles, the length of time the material is frozen, or the air temperature (Grossi, et al., 2007). Hama et al. (1999) and Noguchi and Hama (2021) related environmental factors to the number of freeze-thaw cycles specified in ASTM C666 A method (2015) to predict durability of a material under weather conditions based on the freeze-thaw test results. In addition, damage functions such as the modified version of the winter index (MWI), time of frost (TOF), amount of water (ASW), and indicative freeze-thaw cycles (IFTC) were used with hygrothermal simulation tools to compare the risks of frost damage to building walls with different envelope types or in different climates (Kočí, et al., 2017; Kočí, et al., 2018). Zhou et al. (2017) proposed the FTDR index based on the amplitude of the ice saturation degree of a building wall. This index is calculated using a hygrothermal simulation that includes freezing and thawing processes, and its concept reflects the characteristics of freeze-thaw cycles in a real environment, where freezing often resumes before thawing is complete.

These approaches are well suited for comparing the risks of building deterioration under different climatic conditions or with different wall structures. At present however, the mechanisms of frost damage under weather conditions are not well understood, and there appears to be a variety of phenomena that need to be uncovered for a more reliable assessment. For one of these phenomena, Nakamura et al. (2011a; 2011b; 2016) proposed “blockage-type” freeze-thaw cycles, in which cyclic freezing and thawing creates an unfrozen area surrounded by a frozen area inside a material. The frozen area traps the unfrozen water inside and results in destructive pressure associated with volume increase due to freezing. This mechanism is similar to the closed container theory (Fagerlund, 1997), which describes the increase in pressure in a low permeability material that prevents unfrozen water from escaping from the material as the water volume increases due to freezing. In contrast, freezing originating from the material surface blocks the movement of unfrozen water from the inside in the “blockage-type” freeze-thaw cycles, rather than the low permeability of the material.

Similar effects blocking water movement in a material have been observed in freeze-thaw tests. Wardeh and Perrin (2008) and Sánchez de Rojas et al. (2011) discussed the effects of a wet cloth

54 placed on a roof tile specimen on the results of freeze-thaw tests using method E specified in the
55 European standard (DIN EN 539-2, 2013) by comparing tests with and without a wet cloth [1]. The
56 explanation is as follows. Because the wet cloth contains a large amount of water, a specimen surface
57 in contact with the cloth freezes first during a cooling period and blocks the movement of water toward
58 it, which increases the internal pressure and leads to greater stress and damage. In fired clay materials
59 such as roof tiles and bricks, the likelihood of "blocking" type freeze-thaw cycles appears to be high
60 because the freezing point depression of the contained water in these materials is low due to the large
61 pore diameters and freezing progresses rapidly slightly below 0 °C, resulting in severe blocking of the
62 movement of unfrozen water. However, the significance of the “blockage-type” freeze-thaw cycles
63 for pressure development in real buildings or structures has not yet been clarified because it is difficult
64 to adequately reflect real weather conditions in laboratory experiments.
65 Therefore, in this study, we aim to demonstrate the pressure evolution of trapped pore water during
66 cyclic freezing and thawing under real weather conditions. To decipher the complex interaction
67 between heat and moisture transfer and pressure change in a material induced by environmental
68 condition changes, we used coupled hygrothermal and mechanical simulations that consider freezing
69 and thawing processes based on the theory of poromechanics (Coussy, 2004; Coussy, 2005; Coussy &
70 Monteiro, 2008). The rest of this study is organized as follows. In the second section, we summarize
71 the studies by Nakamura et al. (2011a; 2011b; 2016) to clarify the environmental conditions that lead
72 to degradation by “blockage-type” freeze-thaw cycles. In the third section, a coupled hygrothermal
73 and mechanical model is developed, and its validity is confirmed by comparing the calculation results
74 with the results of strain measurements on a brick specimen. Finally, in the fourth section, calculations
75 are performed to demonstrate the effects of water blockage. We performed two calculations in which
76 a material was subjected to multiple freeze-thaw cycles. In the first calculation, a material was exposed
77 to a relatively simple temperature variations of the outside air. In contrast, real meteorological data
78 (air temperature and solar radiation) in a cold region were input into the second calculation.

[1] Wardeh & Perrin (2008) compared tests with and without wet cloth using the temperature conditions specified in the E method of EN 539-2. Sanchez de Rojas et al (2011) compared experiments using the C and E methods of EN 539-2.

2. Observation of the deterioration of brick walls in the literature

Nakamura et al. (2011a; 2016) reported the deterioration of brick walls in Kitami City, Hokkaido Prefecture, Japan. Fig. 1 shows the daily average temperature, humidity, and hourly snow depth in the region in 2020 provided by the Japan Meteorological Agency (2021). Humidity data in Kitami City are not provided. Instead, data are shown for the neighboring city of Abashiri, which is about 40 km from Kitami City. The region is classified as a humid continental climate zone according to the Köppen climate classification (Kottek, et al., 2006), and is characterized by low temperatures and continuous snow cover in winter.

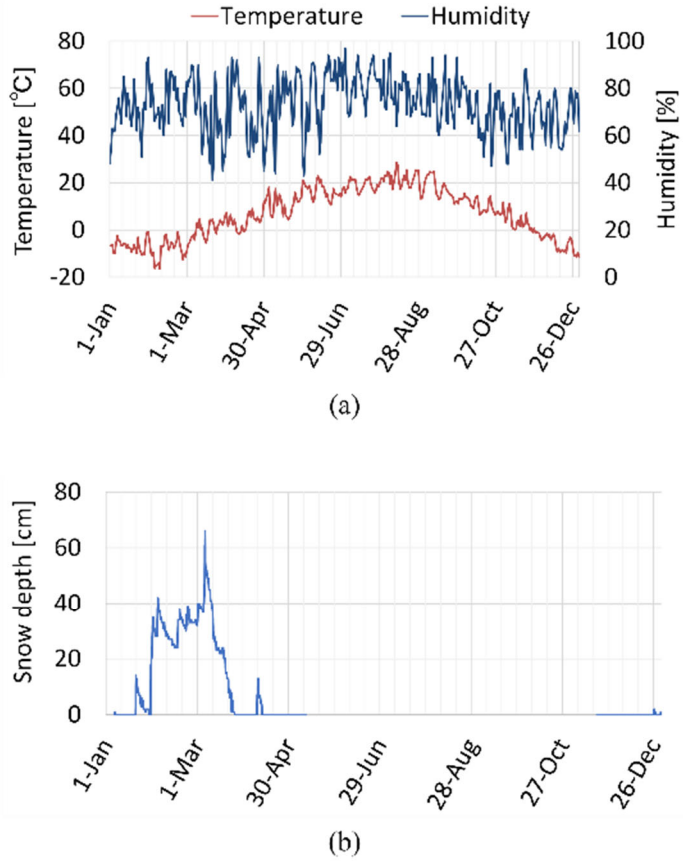

Fig. 1. (a) Daily average temperature and humidity and (b) hourly snow depth in the region including Kitami City.

93 The brick walls are 130 cm high and are located near the Japan Railway (JR) Kitami Station. Fig.
94 2 (a) shows an aerial photograph of the walls and station taken in 2015 (Geospatial Information
95 Authority of Japan, 2021). The walls surround a parking lot and, therefore, are oriented in different
96 directions. The observations of Nakamura et al. (2011a) can be summarized as follows:
97 • There were many cracks, including fatal ones, and flaking on the south facing walls, whereas tiny
98 cracks were observed on the north facing walls.
99 • Most of the damage was observed on the bricks at the top of the walls, as shown in Fig. 2 (b),
100 where the bricks were most exposed to the external environment.
101 • They conducted measurements of the temperatures of outside air and the on the surface and
102 outside temperature of the brick walls. Based on the measurement results in late winter, the
103 surface temperature of the south facing wall can reach 30 °C due to solar radiation. Therefore, it
104 is assumed that the bricks are subject to a cycle of thawing during the day and freezing at night.
105

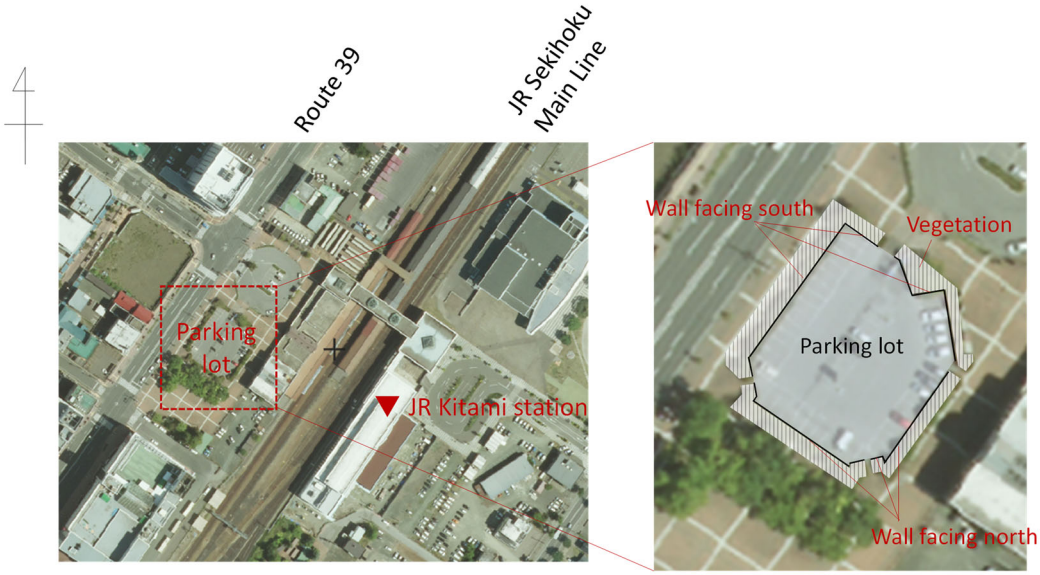

(a)

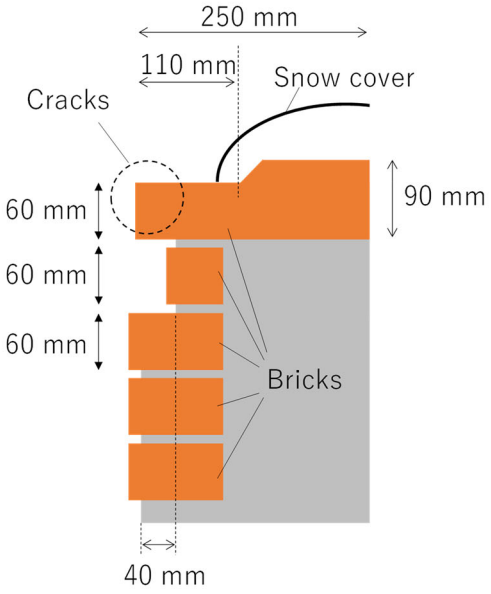

(b)

Fig. 2 (a) Aerial photograph of the parking lot with brick walls (Geospatial Information Authority of Japan, 2021) (retouched by the authors) and (b) schematic cross-section of the brick wall (prepared by the authors with reference to Nakamura, et al. (2011a)).

Nakamura et al. (2011b; 2016) also conducted laboratory experiments to investigate the causes of the deterioration. In their experiment, brick specimens were exposed to either of two patterns of freeze-

thaw cycles. While the first experiment was an ordinary one-dimensional freeze-thaw test, in the second experiment they used a special temperature condition to simulate freeze-thaw cycles under real weather conditions in a cold region. The assumption was that the bricks began to thaw from the surface during the day due to solar radiation, but the interior remained frozen, resulting in a significant increase in the water pressure as the unfrozen water became trapped by frozen zones when freezing resumed on the surface the next night. Fig. 3 shows schematic representations of the freeze-thaw processes during the second experiment. At the end of the cooling period, the specimens were completely frozen (Fig. 3 (a)) and gradually thawed at the surface during the heating period (Fig. 3 (b)). However, the next cooling period started before the specimen was completely thawed (Fig. 3 (c)), and an unfrozen zone surrounded by frozen zones formed inside (Fig. 3 (d)). In their experiment, the minimum temperature was set at −8, −15, and −25 °C, and the maximum temperature was set at 20 ± 5 °C. The second cooling period started when the temperature became positive at a distance of 10 mm or 60 mm from the surface. They showed that cracks appeared only after the second freezing in the second experiment, while the one-dimensional freeze-thaw test did not cause such deterioration. Therefore, they concluded that just one "blockage-type" freeze can be very damaging to the materials.

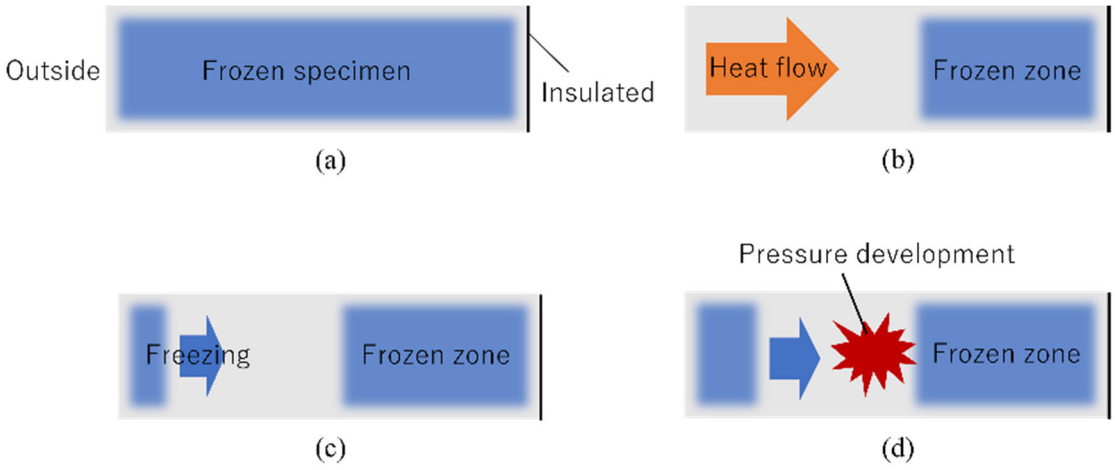

Fig. 3. Schematic representation of the freezing and thawing processes during the "blockage-type" freeze-thaw experiment performed by Nakamura et al. (2011b; 2016).

Although Nakamura et al. (2011a; 2016) did not observe building envelopes, the brick walls were exposed to very common environmental conditions in cold regions, and there were many similarities in boundary conditions with building envelopes. In addition, Takami and Ishizaki (2012) observed that a building brick wall was more seriously damaged by frost action in the same climate zone (Otaru, Hokkaido Prefecture, Japan) when exposed to sunlight. Therefore, it is very likely that the building walls are damaged by mechanisms similar to those studied by Nakamura et al. (2011a; 2016)

3. Coupled hygrothermal and mechanical model

3.1. Fundamental equations

3.1.1. Constitutive equations

In this study, we have assumed that the materials are nearly saturated with liquid water and ice due to the continuous water supply from the snow cover. Plastic deformation of a material is not considered in the calculations. We used the following constitutive equations for saturated and frozen materials based on the theory of poromechanics (Coussy, 2004; Coussy, 2005; Coussy & Monteiro, 2008):

$$\boldsymbol{\sigma} = \mathbf{D}\left[\boldsymbol{\varepsilon} - \alpha\left(T - T_r\right)\mathbf{I}\right] - b\left(S_i P_i + S_l P_l\right)\mathbf{I} \tag{1}$$

$$\varphi_i = b\varepsilon_{vol} S_i + \frac{P_i}{N_{ii}} + \frac{P_l}{N_{il}} - a_i\left(T - T_r\right) \qquad \varphi_l = b\varepsilon_{vol} S_l + \frac{P_i}{N_{li}} + \frac{P_l}{N_{ll}} - a_l\left(T - T_r\right) \tag{2}$$

where a_j is a coefficient related to the volumetric thermal expansion of the pore volume occupied by phase j ($j = i$ or l) [K^{-1}]; b is the Biot coefficient; N_{ii}, N_{il}, N_{li} and N_{ll} are the generalized Biot coupling moduli [Pa]; P is the pressure [Pa]; S is the saturation; T is the temperature [K]; T_r is the reference temperature [K]; α is the thermal expansion coefficient of the skeleton [K^{-1}]; ε_{vol} is the volumetric strain; φ_j is the increment of porosity occupied by phase j ($j = i$ or l); $\mathbf{D}$ is the elastic stiffness tensor of the material [Pa]; $\boldsymbol{I}$ is the second order unit tensor, $\boldsymbol{\varepsilon}$ is the strain tensor; and $\boldsymbol{\sigma}$ is the total stress tensor [Pa]. The subscripts i and l represent the ice and liquid water, respectively. Eqs. (1) and (2)

158 represent the deformation of the material and pore space, respectively due to the pressure changes of
159 the liquid and ice phases as well as the thermal expansion and external force. Unlike our previous
160 study (Fukui et al., 2023a), the model did not consider the anisotropy of the material properties, for
161 simplicity. Therefore, the thermoporoelastic material properties can be derived using the following
162 equation (Coussy, 2005; Coussy & Monteiro, 2008):
163
164 $$b = 1 - \frac{K}{K_s} \tag{3}$$
165 $$\frac{1}{N_{ii}} + \frac{1}{N_{il}} = \frac{b-\phi_0}{K_s} S_i \qquad \frac{1}{N_{li}} + \frac{1}{N_{ll}} = \frac{b-\phi_0}{K_s} S_l \tag{4}$$
166 $$a_j = 3\alpha \left(b - \phi_0\right) S_j \qquad j = i, l \tag{5}$$
167
168 where K and K_s are the bulk moduli of the bulk material and its solid phase, respectively, and ϕ_0 is the
169 porosity in the reference state. According to Aichi and Tokunaga (2011), the following equations were
170 used to calculate N_{ii}, N_{il}, N_{li} and N_{ll}:
171
172 $$\frac{1}{N_{ii}} = \frac{b-\phi_0}{K_s} S_i^2 \quad \frac{1}{N_{il}} = \frac{1}{N_{li}} = \frac{b-\phi_0}{K_s} S_j S_l \quad \frac{1}{N_{ll}} = \frac{b-\phi_0}{K_s} S_l^2 \tag{6}$$
173
174 As b, K_s, α, and ϕ_0 are constants, S_j is only a variable to derive the poroelastic parameters b, N_{ii}, N_{il},
175 N_{li}, N_{ll}, and a_j. S_j is time and space dependent and determined based on the relationship described in
176 subsection 3.1.2. Using S_j for each time step and element, the poroelastic parameters were determined.
177
178 *3.1.2. Equilibrium relationships between ice and liquid water*
179 Assuming thermodynamic equilibrium conditions between the ice and liquid water in the pores, the
180 following Clausius-Clapeyron equation was used (Coussy & Monteiro, 2009):
181

$$\frac{P_l}{\rho_l} - \frac{P_i}{\rho_i} = \frac{\Delta s}{\rho_i}\left(T - T_m\right) \tag{7}$$

where T_m is the melting point of bulk water [K], Δs is the melting entropy (= 1.2 [MPa/K]), and ρ is the density [kg/m^3]. The dependence of the density of water on pressure and temperature is expressed by the following linearized form (Coussy, 2005; Coussy & Monteiro, 2008):

$$\frac{1}{\rho_j} = \frac{1}{\rho_j^0}\left(1 - \frac{P_j}{K_j} + 3\alpha_j\left(T - T_r\right)\right) \quad j = i, l \tag{8}$$

where ρ_j^0 is the density of phase j ($j = i$ or l) in the initial state [kg/m^3].

To express the relationship between pore water pressure and saturation, the well-known form proposed by van Genuchten (1980) was applied to the freezing and thawing processes, taking into account the difference in interfacial energy (Zeng, et al., 2011):

$$S_l = \left[\frac{1}{1 + \left(\beta \frac{\gamma_{al}}{\gamma_{il}}\left(P_i - P_l\right)\right)^n}\right]^m \tag{9}$$

where n, m, and β are constants, and γ_{al} and γ_{il} are the interfacial energies between air and liquid water (= 73 × 10^{-3} [J/m^2] at 20 °C) and between ice and liquid water (= 33 × 10^{-3} [J/m^2] at 0 °C), respectively.

3.1.3. Conservation equations

The conservation equations used in this study are the same as those used in our previous study (Fukui et al., 2023a), but the anisotropy of the material properties was ignored for simplicity. The momentum balance is expressed as follows:

$$\nabla \cdot \boldsymbol{\sigma} + \mathbf{F} = 0 \tag{10}$$

where **F** denotes the body force vector [N/m^3]. Assuming that there are no external sources of force, **F** = 0. The equations for heat and moisture conservation are expressed as follows:

$$\frac{\partial}{\partial t}\left(CT - HM_i\right) = \nabla \cdot \left(\lambda \nabla T\right) \tag{11}$$

$$\frac{\partial}{\partial t}\left(M_i + M_l\right) = \nabla \cdot \left(\lambda'_l \nabla P_l\right) \tag{12}$$

where

$$C = c_d \rho_d + c_i M_i + c_l M_l \tag{13}$$

$$M_j = \rho_j \left(\phi_0 S_j + \varphi_j\right) \quad j = i, l \tag{14}$$

where c is the specific heat [J/(kg·K)], H is the latent heat of solidification (334 × 10^3 [J/kg]), λ is the thermal conductivity [W/(m·K)], and λ_l' is the moisture permeability [kg/(m·s·Pa)]. Subscript d represents the bulk material in the dry state. C is the volumetric specific heat of the wet material [J/(m^3·K)] and M_j is the mass of phase j contained in a unit volume of the bulk material [kg/m^3]. When water freezes, the volume increases (which is considered as the density change in the model), and the material deforms in conjunction with an increase in liquid and ice pressures to satisfy the mass balance (Eq. (14)) and the constitutive equations (Eqs. (1) and (2)). In addition, the unfrozen water flows out of the freezing area due to the pressure gradient according to Eq. (14), and the importance of the pressure depends on the moisture permeability.

3.2. Numerical solution

The calculations were performed in two dimensions assuming a plane-strain state. The conservation equations were spatially discretized using Galerkin's finite-element method. T, P_l and the displacement vector **u** [m] were chosen as the main variables and expressed by vectors of nodal values $\mathbf{T_e}$, $\mathbf{P_e}$, and $\mathbf{u_e}$, and linear shape functions **N** and $\mathbf{N_u}$:

$$T = \mathbf{N}\mathbf{T_e} \quad P_l = \mathbf{N}\mathbf{P_e} \quad \mathbf{u} = \mathbf{N_u}\mathbf{u_e} \tag{15}$$

After discretization, we obtain the following system of equations:

$$\begin{bmatrix} \mathbf{C_{TT}} & \mathbf{C_{TP}} & \mathbf{C_{Tu}} \\ \mathbf{C_{PT}} & \mathbf{C_{PP}} & \mathbf{C_{Pu}} \\ \mathbf{C_{uT}} & \mathbf{C_{up}} & \mathbf{C_{uu}} \end{bmatrix} \frac{\partial}{\partial t} \begin{bmatrix} \mathbf{T_e} \\ \mathbf{P_e} \\ \mathbf{u_e} \end{bmatrix} = \begin{bmatrix} \mathbf{K_{TT}} & \mathbf{0} & \mathbf{0} \\ \mathbf{0} & \mathbf{K_{uu}} & \mathbf{0} \\ \mathbf{0} & \mathbf{0} & \mathbf{0} \end{bmatrix} \begin{bmatrix} \mathbf{T_e} \\ \mathbf{P_e} \\ \mathbf{u_e} \end{bmatrix} + \begin{bmatrix} \mathbf{f_T} \\ \mathbf{f_P} \\ \partial \mathbf{f_u} / \partial t \end{bmatrix} \tag{16}$$

where Eq. (10) is differentiated by time after substituting Eq. (1). The components **C** and **K** were described in our previous study (Fukui et al., 2023a). The finite difference method was used for the discretization in time, and the fully implicit method was used.

3.3. Model validation

3.3.1. Strain measurement

Strain measurement results reported in the previous study (Fukui et al., 2023b) were used for model validation. The measurement was performed under simple boundary conditions and was suitable to capture the deformation caused by the pressure evolution due to freezing and thawing. No constraining force was applied to the specimen. The measurement method is as follows. A brick specimen manufactured in Aichi Prefecture, Japan, was used. The bricks had dimensions of 210 mm × 100 mm × 60 mm. To reduce the three-dimensional effects of heat and moisture transfer in the specimen as

much as possible, the measurements were made in the center of the 210 mm long sides, as shown in Fig. 4. A strain gage (KFLB-5-120-C1-11 R3M3, Kyowa Electronic Instruments Co., Ltd.) was placed in the center of the 210 mm × 60 mm top surface and a thermocouple was attached nearby with a cyanoacrylate adhesive. The direction in which the strain was measured is the same as the height direction of the brick wall shown in Fig. 2 (a). Strain and temperature were also measured on one of the 210 mm × 100 mm side surfaces (not shown in the figure). The specimen was vacuum-saturated and covered with polyvinylidene chloride wrap to prevent evaporation from the surfaces of the specimen before the measurement. It was assumed that the wrap would not exert any constraining forces on the deformation of the specimen and would allow the liquid water to extrude through the surfaces of the specimen. The specimen was frozen and thawed in a climatic chamber. The air temperature in the chamber was maintained at −10 and 20 °C during the cooling and heating periods, respectively. The duration of the cooling and heating periods was 21 h and 15 h, respectively, and the rates of temperature change were not controlled. Before the cooling period, the air temperature in the chamber was kept at 20 ℃ for one hour to stabilize the temperature of the specimen.

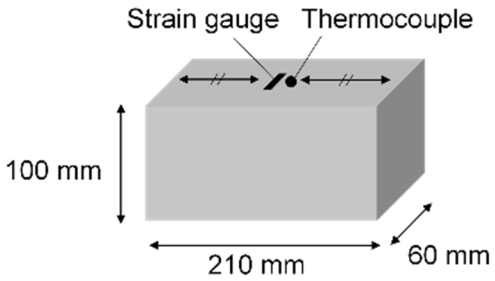

Fig. 4. Schematic diagram of a brick specimen for strain measurement for model validation

3.3.2. Calculation model and conditions

Fig. 5 shows a schematic representation of the calculation model for the strain measurement. The model corresponded to the 100 mm × 60 mm cross section in the middle of the 210 mm long side of the brick specimen for the strain measurement shown in Fig. 4. The calculation was performed for a

quarter of the cross-section because the specimen was symmetrical. The plane strain condition was assumed. We used square elements with 2.5 mm edges and set the time step to 10 s in this calculation. The initial temperature in the material was uniform and set to the average of the temperatures measured on the top and side surfaces at the beginning of the experiment. One hour before the cooling period was included in the calculation. As the specimen was saturated with liquid water at the beginning of the experiment, the initial value of P_l in the material was set to 0 Pa. There was no heat or moisture flux on the axes of symmetry ($x = 0$ or $y = 0$ in Fig. 5) and the displacement normal to the axis directions was restricted. On the surfaces of the material, P_l was set to 0 Pa and the heat flow was calculated using the Robin boundary condition with the measured air temperature in the test chamber. The heat transfer coefficient between the material surfaces and the air in the chamber was determined to be 9.0 [W/(m^2·K)] based on the rate of temperature decrease before the onset of freezing in the cooling period.

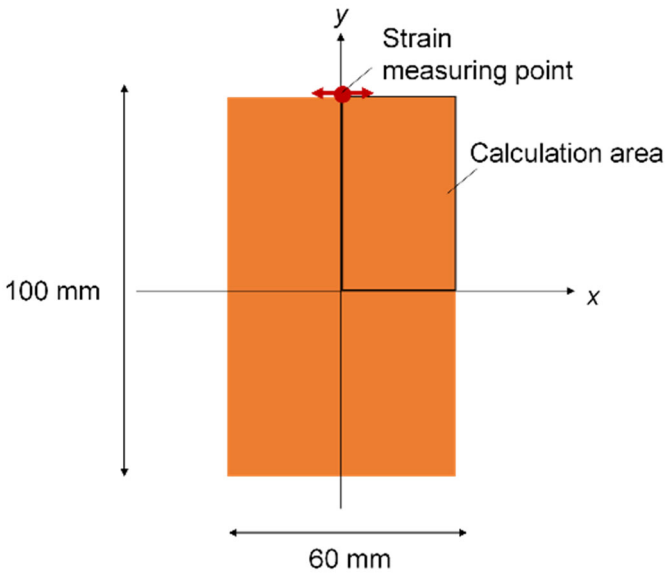

Fig. 5. Calculation model of a brick specimen for strain measurement for model validation

3.3.3. Material and water properties

Based on laboratory measurements and the literature, the parameters listed in Table 1-3 were used for the calculations. The temperature dependence of the properties was neglected in the calculations because it was much less significant than the dependence on water saturation. The water retention

294 curve and thermal conductivity of the material in the unfrozen and unsaturated states were derived
295 from the literature (Kumaran, 1996) and approximated using van Genuchten's equation (Van
296 Genuchten, 1980) and a linear function, respectively, as shown in Fig. 6. The parameters in Eq. (9)
297 were determined as follows: β = 0.0000357, n = 1.52, and m = 0.342. The dependence of thermal
298 conductivity on ice saturation was estimated using Maxwell's equation, (de Vries, 1963) as in our
299 previous study (Fukui, et al., 2021):
300
301 $$\lambda = 1.0 + \phi_0 \left(4.18 S_l + 7.15 S_i \right) \tag{17}$$
302

303 **Table 1.** Material properties with a constant value used in the calculations.

Property	Unit	Symbol	Value	Source
Dry density	kg/m^3	ρ_d	1940	Measurement
Water content at vacuum saturation*	m^3/m^3	ϕ_0	0.246	Measurement
Specific heat	J/(kg·K)	c_d	920	Literature (Kumaran, 1996)
Vapor permeability**	kg/(m·s·Pa)	μ	2.6×10^{-11}	Literature (Kumaran, 1996)
Thermal expansion coefficient	K^{-1}	α	3.8×10^{-6}	Measurement
Young modulus***	Pa	E	19×10^9	Measurement
Poisson's ratio***		ν	0.32	Measurement
Biot coefficient		b	0.57	Eq. (7)

304 *regarded as the open porosity

305 **used to derive the moisture permeability (Eq. (21))

306 ***used to calculate the elastic stiffness tensor **D** and bulk modulus K in Eqs. (1) and (3), respectively.

307

308 **Table 2.** List of hygrothermal and poroelastic parameters used in the calculations, given as a function.

Property	Unit	Symbol	Figure	Equation
Thermal conductivity	W/(m·K)	λ	Fig. 6 (b)	Eq. (17)
Water retention curve			Fig .6 (a)	Eq. (9)
Moisture permeability	kg/(m·s·Pa)	λ’	Fig. 7 (b)	Eq. (18)
Generalized Biot coupling moduli	Pa	N_{ii}, N_{il}, N_{li}, N_{ll}		Eq. (4)
Coefficient related to the volumetric thermal expansion of the pore volume	K^{-1}	a_i, a_l		Eq. (5)

309

310

311 **Table 3.** List of properties of water used for calculations.

Property	Unit	Symbol	Value		Source
			Liquid water	ice	
Specific heat	J/(kg·K)	c	4.22×10^3	2.117×10^3	
Bulk modulus	Pa	K	1.79×10^3	7.81×10^3	Literature (Coussy, 2005; Coussy & Monteiro, 2008)
Coefficient of thermal expansion	K^{-1}	α	-95.4×10^{-6}	51.7×10^{-6}	Literature (Coussy, 2005; Coussy & Monteiro, 2008)
Density in reference state	kg/m^3	ρ^0	1000	917	

312

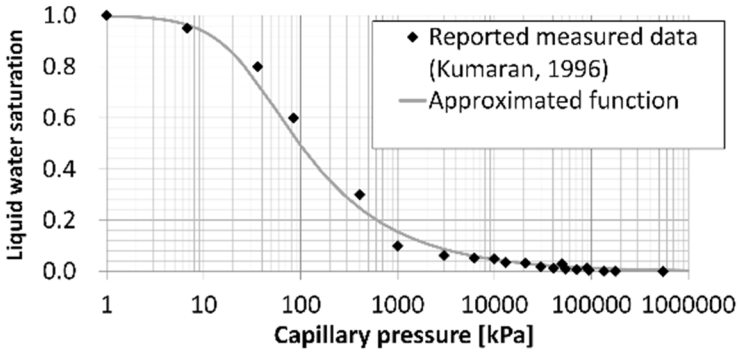

(a)

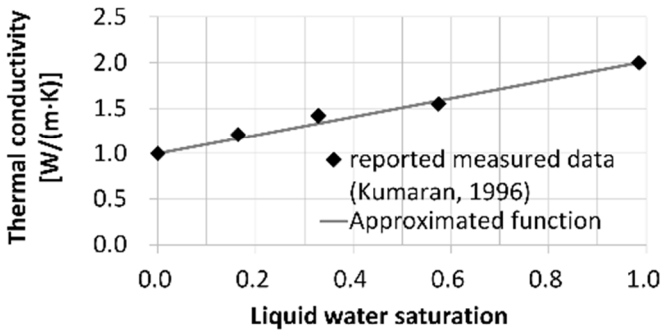

(b)

313

314 **Fig. 6.** (a) Water retention curve and (b) thermal conductivity of a brick in the unfrozen and
315 unsaturated state

316

317 The moisture diffusivity derived using the ruler method (Evangelides, et al., 2018; Ren, et al.,
318 2019) is shown in Fig. 7 (a). We assumed that the water uptake surface was capillary-saturated during
319 the measurement. To extend the obtained function to the vacuum-saturated region, we assumed that
320 the moisture diffusivity did not change significantly between the capillary and vacuum-saturated states
321 (represented by the dotted line in Fig. 7 (a)). From the moisture diffusivity function and water
322 retention curve, the moisture permeability of the unfrozen material was calculated using the
323 following equation:

324

$$\lambda' = \rho_l \phi_0 D_w \frac{\partial S_l}{\partial P_c} \tag{18}$$

325

where D_w is the moisture diffusivity [m^2/s] and P_c is the capillary pressure [Pa]. The derivation of a moisture transport coefficient using the moisture diffusivity and water retention curve is valid in the capillary water region (Künzel, 1995). However, in the low liquid water saturation region, the vapor transport is dominant at normal temperature, which should be omitted in the freezing processes of a saturated material.

The vapor pressure can be expressed as follows (Künzel, 1995):

$$P_v = P_{sat} h = P_{sat} \exp\left(\frac{P_c}{\rho_l R_v T}\right) \tag{19}$$

where P_{sat} is the saturated vapor pressure [Pa] and R_v is the gas constant of the vapor [J/(kg·K)]. As P_{sat} is a function of temperature, the vapor flow q_v [kg/(m^2·s)] in a material can be expressed as follows:

$$q_v = -\mu \frac{\partial P_v}{\partial x} = -\mu\left(\frac{\partial P_v}{\partial T}\frac{\partial T}{\partial x} + \frac{\partial P_v}{\partial P_c}\frac{\partial P_c}{\partial x}\right) = -\left(\mu_T \frac{\partial T}{\partial x} + \mu_P \frac{\partial P_c}{\partial x}\right) \tag{20}$$

where P_v is the vapor pressure [Pa], μ is the vapor permeability of the material [kg/(m·s·Pa)], and μ_P and μ_T are the vapor transport coefficients due to capillary pressure and temperature gradient, respectively. To exclude the vapor transfer portion from the total (liquid and vapor) permeability, the following equation was used:

$$\lambda'_l = \lambda' - \mu_P = \rho_l \phi_0 D_w \frac{\partial S_l}{\partial P_c} - \mu \frac{P_v}{\rho_l R_v T} \tag{21}$$

A vapor permeability of 2.6×10^{-11} [kg/(m·s·Pa)] was derived from the literature (Kumuran, 1996). When λ' calculated from Eq. (18) was less than 0, λ'_v was set to 0 [kg/(m·s·Pa)]. The calculated water permeability and its approximated function are shown in Fig. 7 (b). We used this approximated function for the calculations during freezing and thawing, assuming that moisture permeability is similar between the unfrozen and frozen states when the liquid water content was the same (Watanabe & Osada, 2016).

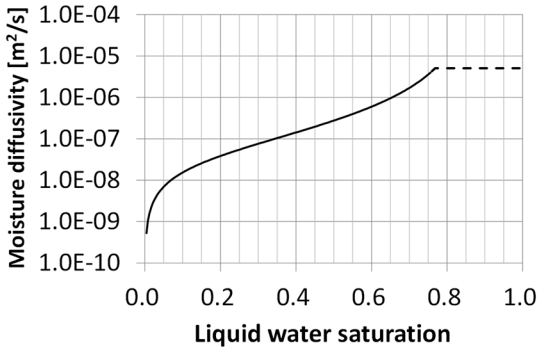

(a)

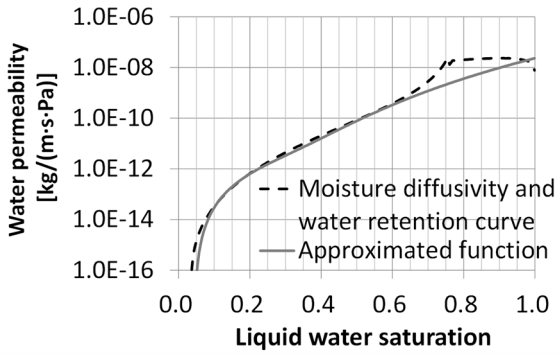

(b)

Fig. 7. (a) Moisture diffusivity and (b) water permeability of a brick.

3.3.4. Comparison of measured and calculated results

Fig. 8 shows a comparison of the measured and calculated temperature and strain evolutions. As shown in Fig. 8 (a), the calculated temperature agrees well with the measured values at the surface of the specimen. The sudden increase in the measured air temperature in the chamber after 18 h was caused by opening the door of the chamber to check the inside. As the anisotropies of the mechanical

properties and Biot coefficient were not considered in the calculation, the calculated strain in the direction normal to the material thickness should be overestimated (Fukui et al,, 2023b). However, the trend of the evolution of the strain was well reproduced in the calculation, except for the decrease after 9 h. The differences in the magnitude of the strain in the calculation and measurement could be due to the imperfection of material properties, especially moisture permeability. The moisture permeability of bricks exhibits large variations and is highly dependent on the liquid water saturation (Kumaran, 1996), which can greatly affect magnitude of the strain. In addition, the decrease in measured strain after 9 h could be due to shrinkage due to the lower pressure of liquid water compared to ice (Eq. 7) (Sun and Scherer, 2010). In our calculation, the liquid water pressure on the boundary was fixed at 0 Pa. Therefore, the pressure of the ice and liquid water was always positive or equal to 0 Pa, and no shrinkage could occur on the material surface in the calculation. However, there also should be an ice phase on the boundary, and it is also possible that the surface had dried slightly after complete saturation. The treatment of the boundary for the calculation of the freezing processes should be investigated in the future. Considering the strain as a function of temperature (see Fig. 8 (c)), there is a relatively large difference between the measured and calculated results. This difference was probably caused by the three-dimensional effects of heat and moisture transfer and deformation. The strain remaining after thawing was the residual strain, which cannot be reproduced in our calculation because plastic deformation was not considered.

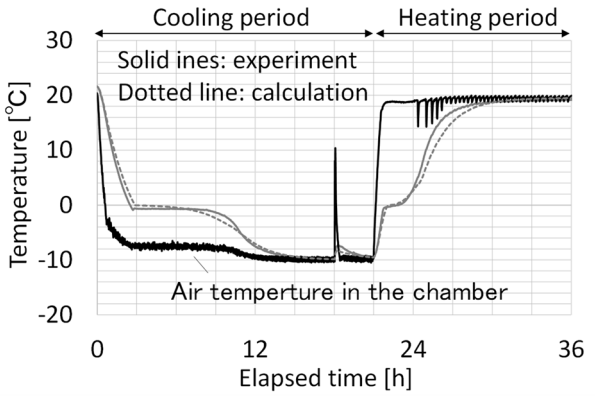

(a)

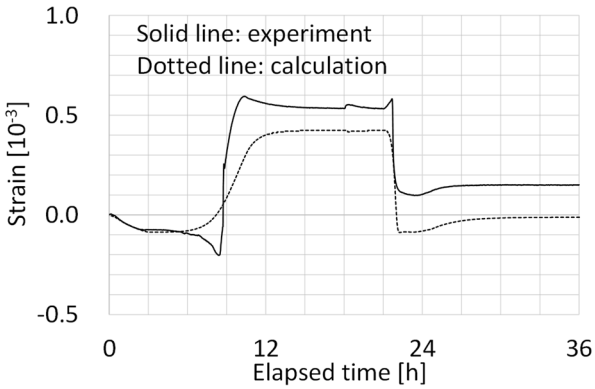

(b)

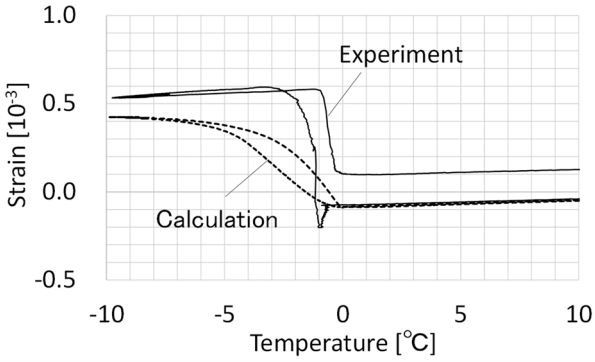

(c)

383

384 **Fig. 8.** Comparison between measured and calculated results; time evolution of the (a) surface

385 temperature and (b) strain, and (c) strain as a function of temperature

386

4. Pressure development during cyclic freezing and thawing

4.1. Calculation methods

4.1.1. Calculation models

In this section, we describe two calculation cases. Fig. 9 shows the calculation model. The model corresponded to the cross section of the top brick of the wall, where the cracks were observed, as shown in Fig. 2 (b). The length of the models was set to 240 mm, which was close to the value given by Nakamura et al. (2011a; 2016). For case 1, relatively simple conditions were used, which cause one-dimensional heat and moisture transfer in the material. The two long sides (y = 0 and 5 mm) were assumed to be insulated and impermeable to moisture, as shown in Fig. 9 (c). One short side (x = 240 mm) was also insulated assuming that the surface was covered with snow, and the other side (x = 0 mm) was exposed to the temperature variations of the outside air (described in the next subsection). The heat transfer coefficient between the material surface and air was set at 23 W/(m^2·K). It was assumed that the snow does not exert any constraining force on the material and liquid water can move freely through the two short sides, i.e., the pressure of liquid water was kept at 0 Pa on these sides. The model consisted of a single sequence of 5 × 5 mm elements, and the time step was set to 10 s.

For the calculation case 2, the boundary conditions reflected the actual weather conditions. The dimensions of the model are 240 mm × 60 mm. The top brick of the wall has different dimensions from common bricks as shown in Fig. 2 (b), but the simplified dimensions were used in the calculation. As shown in Fig. 9 (d), the conditions on the bottom (y = 60 mm) and one short side (x = 240 mm) were the same as in calculation case 1. However, it was assumed that part of the top side (y = 0 mm and x > 80 mm) was also covered with snow, considering the situation shown in Fig. 2 (b), and the same boundary conditions as on the right side (x = 240 mm) were used. On the left part of the top side (y = 0 mm and x < 80 mm) and the other short side (x = 0 mm), solar radiation and air temperature changes were considered as external conditions. The solar radiation was considered in the form of the equivalent temperature:

$$T_{eq} = T_o + \frac{rJ}{h} \tag{22}$$

where h is the heat transfer coefficient [W/(m^2·K)], J is the solar radiation on the wall surface [W/m^2], r is the solar absorptivity of the material, T_{eq} is the sol-air temperature, and T_o is the outside temperature. h and r were set to 23 [W/(m^2·K)] and 0.6, respectively. The calculation was performed using elements with dimensions 20 mm × 20 mm and a time step of 10 s.

For both calculation cases, the initial temperature, liquid water pressure, and material displacement were set to 0 °C, 0 Pa, and 0 m, respectively. The displacements at the bottom (y = 5) for case 1 and right (x = 240 mm) sides for cases 1 and 2 were constrained in the direction normal to each side.

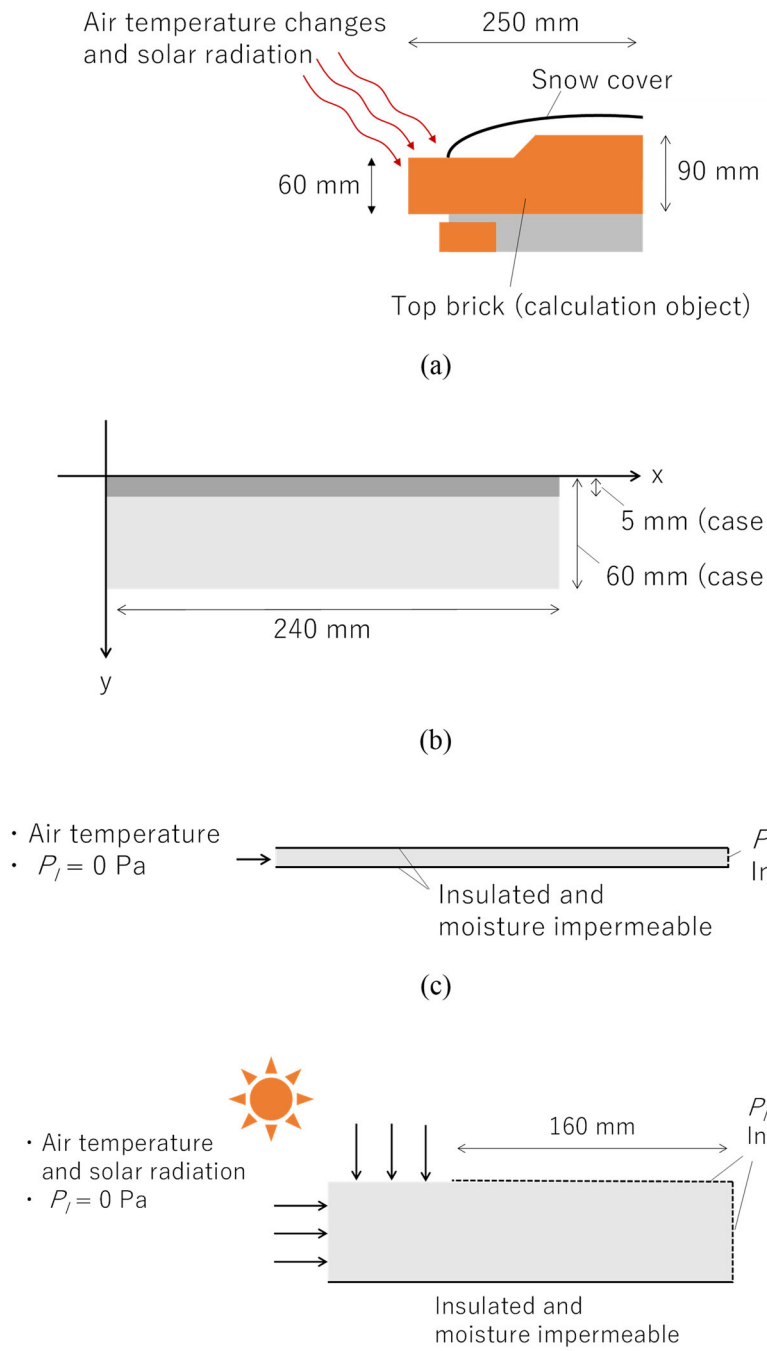

423

424 **Fig. 9.** Schematic diagram of the calculation object and models; (a) the top brick of the wall, (b)

425 simplified dimensions and coordinate system, as well as boundary conditions regarding temperature

426 and water pressure for the calculation (c) case 1 and (d) case 2.

427

428 *4.1.2. External conditions*

429 For the calculation case 1, special temperature condition (see Fig. 10 (a)) was used, which intentionally
430 causes the “blockage-type” freezing. During the first cooling period (with an elapsed time of less than
431 5.25 d), the material was completely frozen. Subsequently, the external temperature increased and
432 reached a maximum of 10 °C during the heating period. At this point, the surface of the material had
433 thawed, but the interior remained frozen. At the beginning of the second cooling period (after six days
434 had elapsed), the outside temperature dropped below 0 °C, and the material began to freeze again. The
435 cooling period was much longer compared with the heating period to ensure complete freezing of the
436 material. These temperature changes during the heating period (5.25-6 d) and at the beginning of the
437 cooling period (6-6.25 d) were sine curve with a wavelength of 1 d simulating the daily temperature
438 fluctuation in a real environment, except for the extra low temperature period (0.25-5.25 and 6.25-12
439 d). These periods were added to ensure the complete freezing of the material. The set maximum and
440 minimum temperatures of 10 and -10 °C, respectively were possible values in Kitami City, considering
441 the air temperature variations in winter (Fig. 1(a)) and temperature increase due to the solar radiation
442 during the daytime.

443 The meteorological data provided by the Japan Meteorological Agency (2021) were entered into
444 the calculation case 2. Fig. 10 (b) shows the hourly temperature changes in Abashiri City. The
445 calculation period was approximately two months, from December 8, 2012 to February 9, 2013, and
446 a run-up period of one week was added before this period. Global solar radiation data were divided
447 into direct and diffuse elements to calculate vertical and horizontal radiation. First, the radiation during
448 the sunny time was expressed using the equations of Bouguer and Berlage as follows:

449

450 $$J_1 = J_0 \tau^{\frac{1}{\sin\theta}} \sin H \tag{23}$$

451 $$J_2 = \frac{1}{2} J_0 \sin\theta \frac{1-\tau^{\frac{1}{\sin\theta}}}{1-1.4\ln\tau} \tag{24}$$

452

where H is the angle between the direct radiation and the surface of the material; J_0 is the solar constant [W/m^2]; J_1 and J_2 are the direct and diffuse solar radiation during the sunny periods [W/m^2], respectively; τ is the atmospheric transmittance; and θ is the solar elevation. We set τ to 0.79. During cloudy periods, the total global solar radiation provided was interpreted as diffuse radiation. Finally, the total radiation was estimated by weighting the solar radiation during sunny and cloudy periods by the daylight duration χ during each hour.

$$J = \chi\left(J_1 + J_2\right) + \left(1 - \chi\right) J_c \tag{25}$$

where J_c is the diffuse radiation during the cloudy period [W/m^2]. Fig. 10 (c) compares the global solar radiation on horizontal surfaces calculated using Eq. (25) with the meteorological data. Both agree well, and we calculated the radiation on the vertical surfaces using Eq. (25), as shown in Fig. 10 (d). In the calculations, we assumed that the vertical surface is oriented to the southeast or northwest. In these two directions, Nakamura et al. (2011a; 2016) compared the degree of degradation to show the effects of solar radiation during the day on pressure development due to cyclic freezing and thawing.

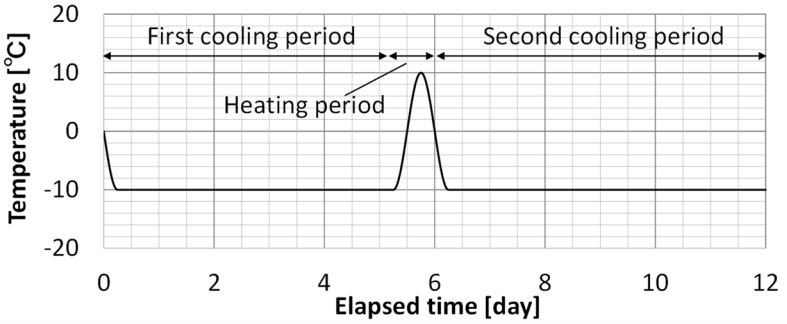

(a)

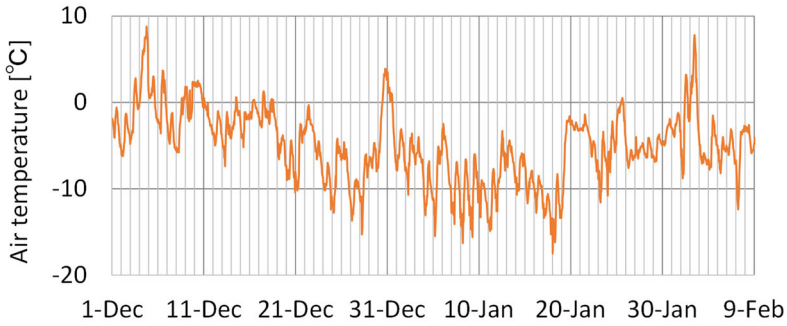

(b)

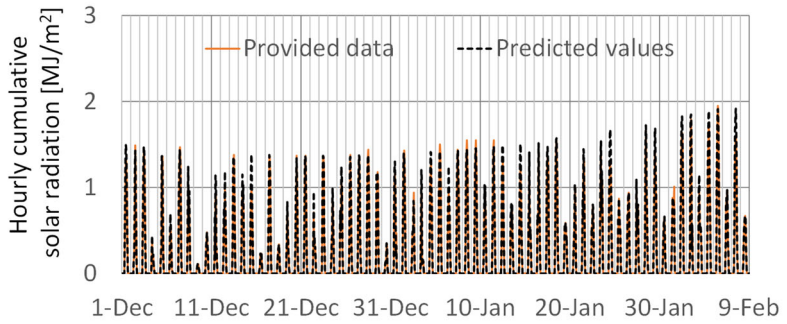

(c)

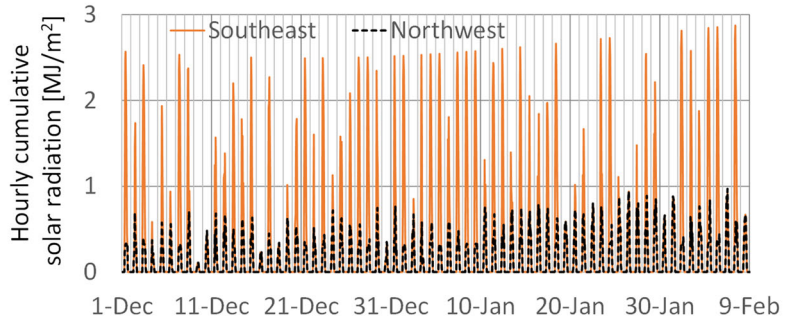

(d)

Fig. 10 External conditions used in the calculations: air temperature for (a) case 1 and (b) case 2, and hourly cumulative solar radiation on (c) horizontal and (d) vertical surfaces for case 2.

4.2. Calculation results and Discussion

4.2.1. Calculation case 1

Figs. 11 and 12 show the time evolution of temperature and liquid water pressure in the material and ice saturation distribution near the external surface immediately after the beginning of the second cooling period, respectively. According to Fig. 11 (a), the surface temperature rose above 0 °C during the heating period (shown with a dotted circle), but the temperature inside the material remained below 0 °C, as intended. Fig. 12 shows that the ice thaws near the surface at the beginning of the second cooling period (after 6 d) and then gradually refreezes from the surface. This creates an area of low ice saturation at a distance of 1 to 2 cm from the surface, indicating that the second freeze is the blocking freeze. Fig. 11 (b) clearly shows that the pressure development in the second cycle was much stronger than that in the first cycle due to water blockage effects, even though the minimum temperature of the material was the same in these two cycles. Note that the pressure of the liquid water sometimes becomes negative because it is always smaller than the pressure of the ice due to the equilibrium relationship (Eq. (7)). During the first freeze, the pressure at the point where x = 16 cm is the highest among the other points in Fig. 11 (b). In contrast, during the second freeze, the pressure tends to be higher in the area near the surface (e.g., at x = 4 and 8 cm) than in the interior of the material. The high pressure observed near the surface during the second freeze is caused by the low ice saturation area (at a distance of 1–2 cm from the surface) during the heating period. The water movement from this area was blocked by the surrounding high ice saturation areas when the water was frozen again from the material surface during the second freeze.

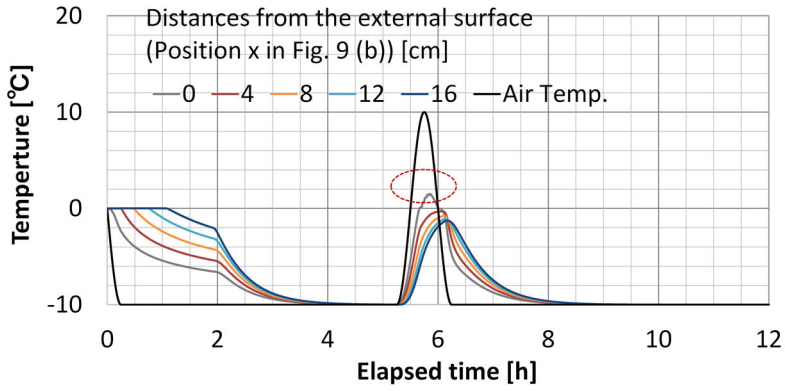

(a)

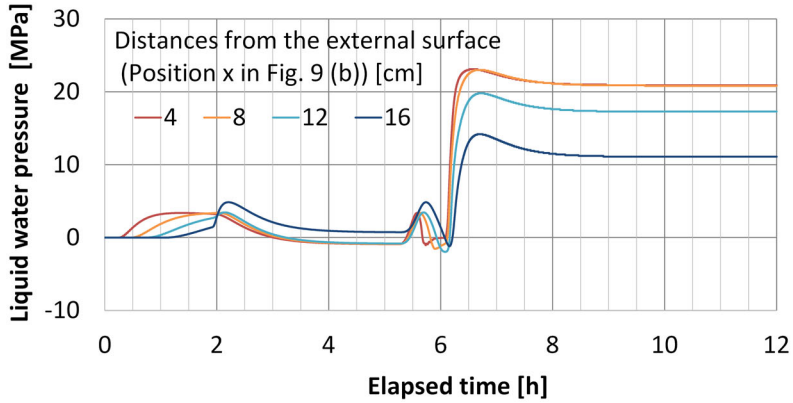

(b)

494

495 **Fig. 11** Calculation results for case 1; evolution of (a) temperature and (b) liquid water pressure

496

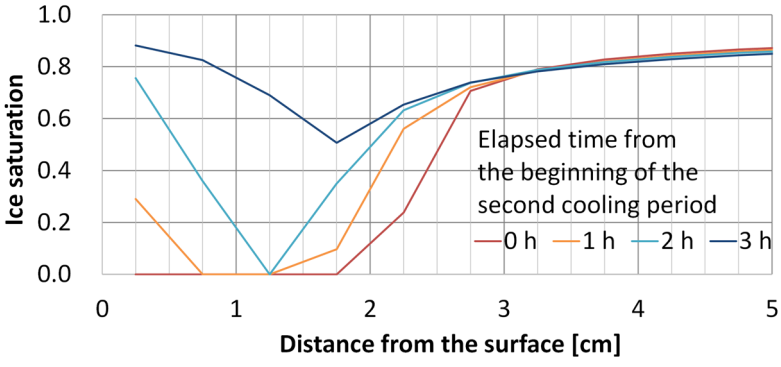

497

498 **Fig. 12** Calculation results for case 1; ice saturation distribution immediately after the start of the

499 second cooling period.

500

501 *4.2.2. Calculation case 2*

502 Fig. 13 shows the calculated results of the temperature and water pressure evolution on the bottom
503 side (y = 60 mm), where the pressure amplitude is the largest. From the comparison of the temperature
504 evolution of the southeast and northwest facing walls (see Fig. 13 (a) and (b), respectively), it can be
505 seen that the temperature on the vertical surface (x = 0 mm) of the southeast facing wall often reaches
506 above 0 ℃ due to solar radiation, whereas such a situation is rare for the northwest facing wall.
507 Therefore, the surface of the southeast facing wall is exposed to significant freezing and thawing cycles.
508 Note that the temperature of the inside of the wall seldom rises above 0 ℃ due to its heat capacity,
509 which means that the inside remains frozen while the surface thaws.

510 These differences in the temperature evolution of the walls oriented to the different directions affect
511 the pressure development in the walls. As can be seen in Fig. 13 (d), the pressure of the liquid water
512 increased to 10 MPa or more in the wall facing the north side. Considering that the tensile strength of
513 conventional bricks is several megapascals, a pressure of this magnitude may cause deterioration of
514 the walls. However, when the pressure development was observed in the wall facing the south side
515 (Fig. 13 (c)), the pressure increased more significantly. These results are consistent with the
516 observations of Nakamura et al. (2011a; 2016) which show that there were tiny cracks on the walls
517 facing the north side and larger and fatal cracks on the walls facing the south side. It is also worth
518 noting that the pressure does not reach its highest value in the middle of February, when the
519 temperature is the lowest. In mid-winter, the temperature cannot be high enough during the day to
520 thaw a sufficient amount of water near the surface to cause the “blockage-type” freeze.

521 Finally, Fig. 14 shows the evolution of the temperature and pressure around December 23 and 24,
522 2012, when the pressure reaches the maximum on the southeast facing wall. On December 23, the
523 temperature near the wall surface was above 0 °C during the day and decreased rapidly during the
524 night. Figs. 15 and 16 show the ice saturation distribution at two time points on December 23 at the
525 southeast and northwest facing wall, respectively. As shown in Fig. 15, the surface of the material was
526 completely thawed at 1 pm and there was an ice saturation gradient in the material. As the wall faces
527 east, it did not receive significant solar radiation in the evening and the surface temperature dropped

528 rapidly (Fig. 14 (b)). Consequently, the area of low ice saturation is clearly visible at a distance of 30
529 mm from the material surface at 4 pm, as shown in Fig. 15 (b). Conversely, the saturation in the wall
530 facing northwest remained high (above 0.75) at 1 pm, and no area of low saturation was formed in the
531 evening. Such a situation is also found on December 20, 21, 22, and 26 but on December 23 the
532 temperature increase during the daytime and decrease at night are relatively large. This means that a
533 large amount of unfrozen water is quickly trapped at night on December 23, resulting in the highest
534 pressure.
535

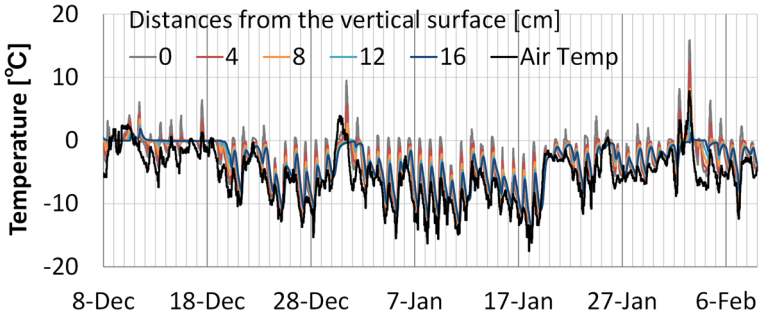

(a)

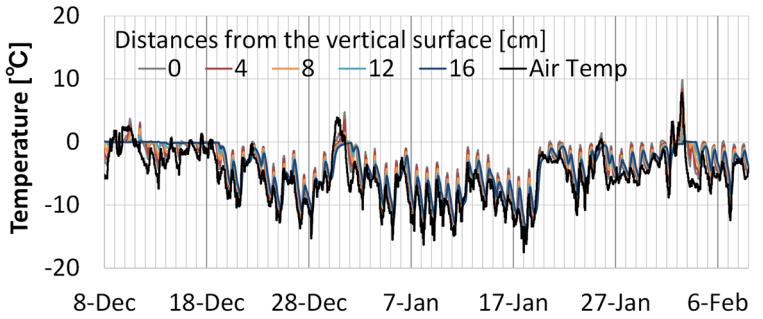

(b)

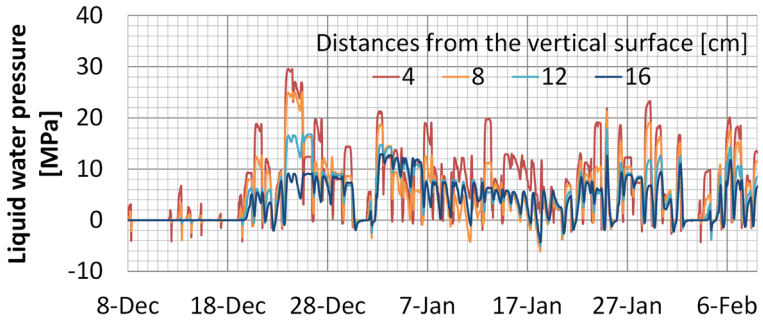

(c)

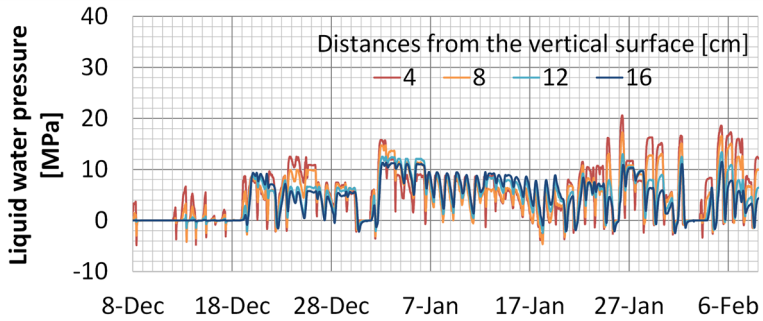

(d)

536

537 **Fig. 13** Calculation results for case 2; temperature evolution in the wall facing (a) southeast and (b)

538 northwest, and the liquid water pressure evolution in the wall facing (c) southeast and (d) northwest.

539

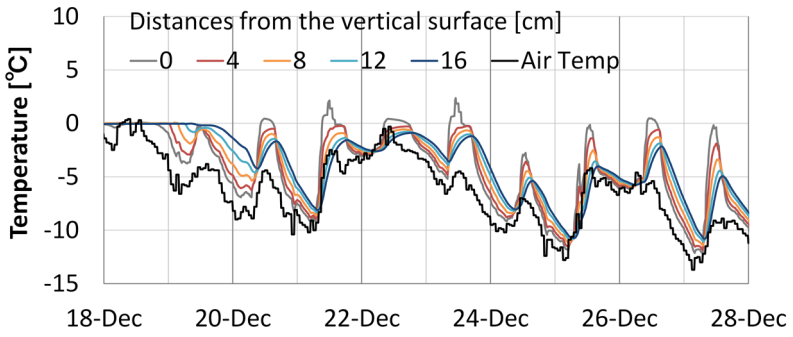

(a)

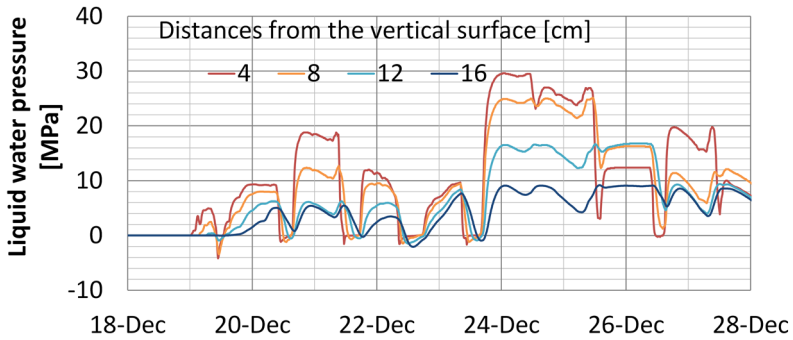

(b)

540

541 **Fig. 14** Calculation results for case 2 from December 18 to 28, 2012; evolution of the (a) temperature

542 and (b) liquid water pressure in the wall facing southeast.

543

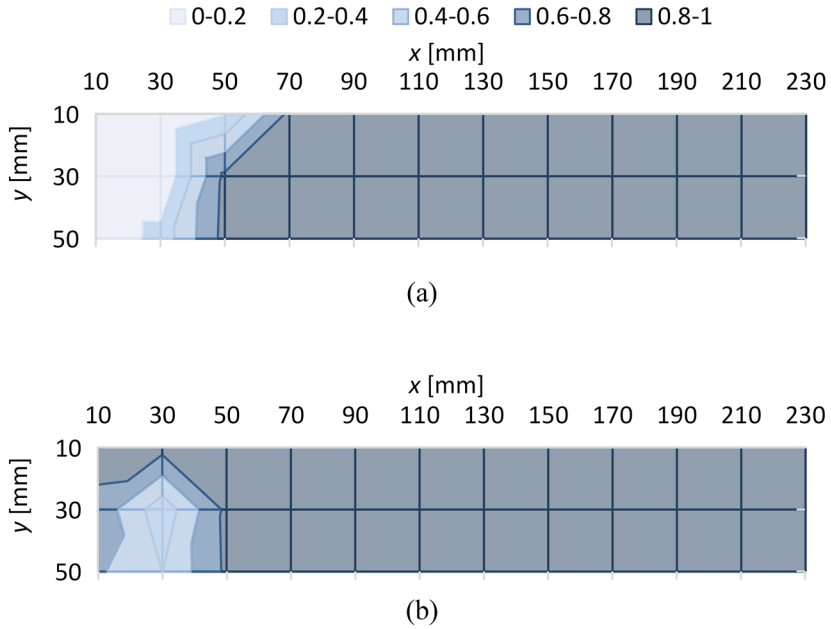

544

545 **Fig. 15** Calculated ice saturation distribution in the wall facing southeast at (a) 1 pm and (b) 4 pm on

546 December 23.

547

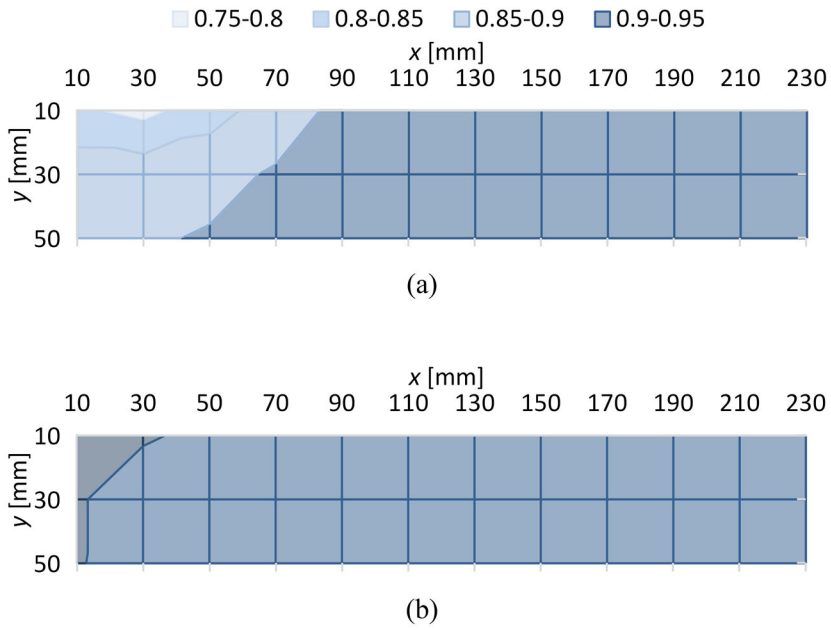

548

549 **Fig. 16** Calculated ice saturation distribution in the wall facing northwest at (a) 1 pm and (b) 4 pm on

550 December 23.

551

552 *4.2.3. Influences of moisture permeability on pressure development in the material*

553 Of the hygrothermal, mechanical, and poroelastic properties used in the calculations, the transport
554 coefficient for liquid water exhibits the greatest variation and strongest dependence on liquid water
555 saturation (Kumaran, 1996). In addition, as water movement in a material plays a key role during the
556 blocking freeze, the pressure development depends strongly on this property. Therefore, an additional
557 calculation was performed with a different moisture permeability to discuss its influence on the
558 pressure development in a material.

559 Fig. 17 shows calculated evolution of the liquid water pressure in the wall facing southeast with
560 the 1.5 times reduced moisture permeability. From the comparison with Fig. 14 (b), the pressure
561 development in the night of December 23 was much more significant than in the original case while
562 the differences in the other periods were smaller. This is because the unfrozen water flow in the
563 material was more blocked when the moisture permeability of the material was low. The hydraulic
564 pressure caused by the unfrozen water flow depends on the moisture permeability of a material
565 (Powers, 1949). The results show that this permeability effect may be more pronounced during the
566 "blockage-type" freezing.

567

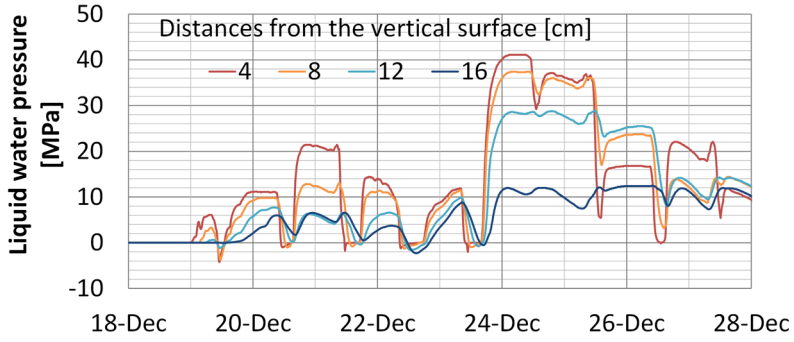

568

569 **Fig. 17** Calculated evolution of the liquid water pressure in the wall facing southeast from December
570 18 to 28, 2012, when moisture permeability was reduced 1.5 times.

571

5. Conclusion

In this study, we investigated the evolution of pore pressure during cyclic freezing and thawing under real weather conditions. The hygrothemal and mechanical simulations clearly showed that the water pressure during a repetition of the freezing and thawing process in which the interior of the material remains frozen, is significantly higher than when freezing from the completely unfrozen state, as is common in ordinary freeze-thaw tests. The calculations for brick walls using meteorological data in a cold region (Kitami City, Hokkaido Prefecture, Japan) showed that for the south facing wall, the surface repeatedly froze at night and thawed during the day, while the inside hardly thawed. Due to these characteristic freeze-thaw cycles, the unfrozen water was trapped in the material and much higher pressure was generated than for the north facing wall. It was also found that the pressure did not reach its highest value, during the coldest part of the winter, because the temperature was too low to cause “blockage-type” freezing.

Our results showed the detrimental effects of “blockage-type” freezing and indicate that the unfrozen water movement in a material significantly influences the evolution of pressure. To avoid the “blockage-type” freeze, it is advantageous for a material to have high water permeability. Materials with fine pores or large porosity are considered to be also less affected by the “blockage-type” freeze as they decrease the rate of the freezing at night due to the significant freezing point depression or large latent heat, respectively.

The limitations of this study are probably due to the boundary conditions of the brick walls considered in this study. Our calculations assumed that the material was covered with snow, which means that the water supply was sufficient. Therefore, the results of this study can be applied to building envelopes with continuous water sources, such as rain, snow, or rising damp. In addition, the constraint forces of the surrounding materials were not considered in the presented calculation. The cases where a material cannot be considered nearly saturated, e.g., because the water sources are not regular, such as condensation, or the surface drying is significant, or where the constraint was considered significant, need to be further investigated, along with modeling the freeze-thaw processes of unsaturated materials.

Acknowledgements/Funding Sources

This work was supported by JSPS KAKENHI Grant Numbers JP19H05511, JP20K04789, and JP21K20462. The authors would like to thank Mr. Suguru Yamanaka for his help in collecting the data of the material properties.

References

Aichi, M. & Tokunaga, T., 2011. Thermodynamically consistent anisotropic constitutive relations for a poroelastic material saturated by two immiscible fluids. *International Journal of Rock Mechanics & Mining Sciences,* Volume 48, pp. 580-84.

ASTM C666, 2015. Standard test method for resistance of concrete to rapid freezing and thawing.

Coussy, O., 2004. *Poromechanics.* Chichester: John Wiley & Sons.

Coussy, O., 2005. Promechanics of freezing materials. *Journal of the Mechanics and Physics of Solids,* Volume 53, pp. 1689-1718.

Coussy, O. & Monteiro, P. J. M., 2008. Poroelastic model for concrete exposed to freezing temperatures. *Cement and Concrete Research,* Volume 38, pp. 40-48.

Coussy, O. & Monteiro, P. J. M., 2009. Errata to 'Poroelastic model for concrete exposed to freezing temperatures'. *Cement and Concrete Research,* Volume 39, pp. 371-72.

de Vries, D. A., 1963. Thermal properties of soils. In: *Physics of Plant Environment.* Amsterdam: North-Holland Publishing Corporation, pp. 210-35.

DIN EN 539-2, 2013. Clay roofing tiles for discontinuous laying - Determination of physical characteristics - Part 2: Test for frost resistance.

Evangelides, C. et al., 2018. Moisture estimation in building materials with a simple procedure. *Construction and Building Materials,* 164(2018), pp. 830-36.

Fagerlund, G., 1997. *Internal frost attack-state of the art: suggestions for future research (Report TVBM (Intern 7000-rapport); Vol. 7110).* Lund: Division of Building Materials, LTH, Lund University.

626 Fukui, K. et al., 2021. Investigation into the hygrothermal behavior of fired clay materials during the
627 freezing of supercooled water using experiments and numerical simulations. *Journal of Building*
628 *Physics,* https://doi.org/10.1177/17442591211041144.
629 Fukui, K. Iba, C., & Ogura, D., 2023a. Deformation of fired clay material during rapid freezing due
630 to supercooling. *Journal of Building Physics,* https://doi.org/10.1177/17442591231154010.
631 Fukui, K. Iba, C., & Ogura, D., 2023b. Coupled hygrothermal and mechanical simulations of highly
632 anisotropic building material during freezing and thawing. *Journal of Building Physics,*
633 (accepted).
634 Geospatial Information Authority of Japan, 2021. [Online] Available at:
635 https://www.gsi.go.jp/top.html [Accessed 28 October 2021].
636 Grossi, C. M., Brimblecombe, P. & Harris, I., 2007. Predicting long term freeze–thaw risks on Europe
637 built heritage and archaeological sites in a changing climate. *Science of The Total Environment,*
638 Volume 377, pp. 273-81.
639 Hama, Y. et al., 1999. Estimation of drost damage of concrete based on meteorological factors. *Journal*
640 *of Structural and Construction Engineering (Transactions of AIJ),* Volume 64, pp. 9-16.
641 Japan Meteorological Agency, 2021 [Online] Available at: https://www.jma.go.jp/jma/index.html
642 [Accessed 28th October 2021].
643 Kočí, J., Maděra, J., Keppert, M. & Černý, R., 2017. Damage functions for the cold regions and their
644 applications in hygrothermal simulations of different types of building structures. *Cold Regions*
645 *Science and Technology,* Volume 135, pp. 1-7.
646 Kočí, J., Maděra, J., Pommer, V. & Černý, R., 2018. Analysis of the frost-induced damage of building
647 enclosures on the territory of the Czech Republic. *Advances in Materials Science and*
648 *Engineering,* Volume 2018, p. 3421801.
649 Kottek, M. et al., 2006. World Map of the Köppen-Geiger climate classification updated.
650 *Meteorologische Zeitschrift,* Volume 15, pp. 259-63.
651 Kumaran, M. K., 1996. *IEA Annex 24, Final Report, Vol. 3, Task 3: Material Properties.* Leuven:
652 Laboratorium Boufysica, Department Burgerlijke Bouwkunde, KU Leuven.

Künzel H M (1995) Simultaneous heat and moisture transport in building components: one- and two-dimensional calculation using simple parameters. Dissertation, Fraunhofer IRB, Germany.

Nakamura, D. et al., 2011a. Frost damage to bricks observed in Kitami City, Hokkaido. *Journal of MMIJ,* Volume 127, pp. 219-29.

Nakamura, D. et al., 2011b. Verification experiment of the mechanism of frost damage to bricks. *Journal of MMIJ,* Volume 127, pp. 256-66.

Nakamura, D. et al., 2016. Elucidation of mechanism of brick wall frost damage at JR Kitami Station. *Journal of MMIJ,* Volume 132, pp. 14-21.

Noguchi, T. & Hama, Y., 2021. Prediction of frost damage considering pore structure change by drying conditions. *Journal of Structural and Construction Engineering (Transactions of AIJ),* Volume 86, pp. 343-51.

Powers, T. C., 1949. The air requirement of frost-resistant concrete. *Proceedings of the Highway Research Board,* vol. 29, pp. 184-211.

Ren, P., Feng, C. & Janssen, h., 2019. Hygric properties of porous building materials (V): Comparison of different methods to determine moisture diffusivity. *Building and Environment,* Volume 164, p. 106344.

Sánchez de Rojas, M. I. et al., 2011. Influence of freezing test methods, composition and microstructure on frost durability assessment of clay roofing tiles. *Construction and Building Materials,* Volume 25, pp. 2888-97.

Sun, Z. & Scherer, G. W., 2010. Effects of air voids on salt scaling and internal freezing. *Cement and Concrete Research,* vol. 40, pp. 260-70.

Takami, M. & Ishizaki, T., 2012. Deterioration of the building materials of otaru branch of Kyu Nihon Yusen building and its protective measures. *Science for conservation,* Issue 51, pp. 77-95.

Van Genuchten, M. T., 1980. A closed-form equation for predicting the hydraulic conductivity of unsaturated soils. *Soil Science Society of America Journal,* Volume 44, pp. 892-98.

Wardeh, G. & Perrin, B., 2008. Freezing–thawing phenomena in fired clay materials and consequences on their durability. *Construction and Building Materials,* Volume 22, pp. 820-28.

680 Watanabe, K. & Osada, Y., 2016. Comparison of hydraulic conductivity in frozen saturated and
681 unfrozen unsaturated soils. *Vadose Zone Journal,* Volume 15, p. vzj2015.11.0154.
682 Zeng, Q., Fen-Chong, T., Dangla, P. & Li, K., 2011. A study of freezing behavior of cementitious
683 materials by poromechanical approach. *International Journal of Solids and Structures,* Volume
684 48, pp. 3267-73.
685 Zhou, X., Derome, D. & Carmeliet, J., 2017. Hygrothermal modeling and evaluation of freeze-thaw
686 damage risk of masonry walls retrofitted with internal insulation. *Building and Environment,*
687 Volume 125, pp. 285-98.
688